Bulletin of Geophysics and Oceanography Vol. 63, n. 4, pp. 575-596; December 2022
DOI 10.4430/bgo00389

Preliminary investigations into two-dimensional aggravation phenomena of seismic ground response in two-layered shallow sedimentary basins

C. Madiai[1,2], G. Ciardi[3], J. Facciorusso[1,2,4], S. Alshoufi[5] and M. Uzielli[1,2,4]

[1] *Department of Civil and Environmental Engineering, University of Florence, Florence, Italy*
[2] *GeoDynamos Joint Laboratory, Florence, Italy*
[3] *Department of Civil and Environmental Engineering, University of Perugia, Perugia, Italy*
[4] *Georisk Engineering S.r.l., Florence, Italy*
[5] *Formerly at the University of Florence, Florence, Italy*

(Received: 12 November 2021; accepted: 30 March 2022; published online: 27 July 2022)

ABSTRACT The influence of local geological and soil conditions on ground motion and earthquake-induced damage is widely recognised, and provisions accounting for local site effects are included in some seismic building codes. However, while most of the standards provide simplified procedures to consider the 1D stratigraphic effects and some also consider 2D effects of surface topography, the effects related to subsurface geometry are essentially neglected. This paper illustrates the main results drawn from an initial investigation into 2D aggravation effects in symmetric basins overlain by two-layered linear visco-elastic deposits. A preliminary investigation is conducted on 2D aggravation factors (*AGFs*), defined as the ratio between the pseudo-acceleration response spectra obtained from 2D and 1D numerical ground response analyses performed on several simplified schemes. The results include: 1) the qualitative visual representation of the relationships between the *AGF* and a set of dimensionless parameters descriptive of basin geometry, stratigraphy, soil properties, and input motion; and 2) the outcomes of a non-parametric statistical test aimed at quantifying the statistical dependency between the *AGF* and the above-mentioned dimensionless parameters. Useful indications are obtained for carrying out subsequent analyses aimed at the development of simplified procedures for the inclusion of basin effects in design codes.

Key words: ground response, 2D site effects, aggravation factor, sedimentary basins, statistical dependency.

1. Introduction

The effects of local site conditions on seismic ground motion have been investigated for almost two centuries. The earliest studies were essentially qualitative, resulting from field observations and relating the building damage to local soil conditions (Mallet, 1862). Subsequent research based both on microseisms and strong motion recordings showed that ground motion is significantly affected not only by the characteristics of the vertical soil profile, but also by topography (e.g. Trifunac and Hudson, 1971; Davis and West, 1973) and basin geometry (Hanks, 1975; Tucker and King, 1984; Zahradnik and Hron, 1987; Rial *et al.*, 1992; Chávez-García *et al.*, 1999; Frankel *et al.*, 2001; Cornou *et al.*, 2003; Bindi *et al.*, 2011; Ktenidou *et al.*, 2016; among

others). Regarding the latter, it is generally accepted that two-dimensional (2D) mechanisms of basin resonance, deflection of body waves at the basin edges, and generation and reflection of surface waves at the basin edges (Zhu *et al.*, 2018a) can produce greater amplitude and longer duration of the ground motion than those predicted by considering one-dimensional (1D) stratigraphic effects alone (Koketsu and Kikuchi, 2000; Zhu *et al.*, 2020). More generally, many studies have observed that the frequency content (and hence the response spectra of surface motions) can be significantly different from those obtained by referring to 1D conditions, either relying on idealised simplified models (e.g. Bard and Bouchon, 1980a; Kawase and Aki, 1989; Pitarka *et al.*, 1996; Semblat *et al.*, 2002; Makra *et al.*, 2005; Khanbabazadeh and Iyisan, 2014; Pitilakis *et al.*, 2015; Zhu and Thambiratnam, 2016) or on actual case studies (e.g. Kawase, 1996; Graves *et al.*, 1998; Bakir and Özkan, 2002; Semblat *et al.*, 2005; Lanzo and Pagliaroli, 2009; Madiai and Simoni, 2013; Vessia and Russo, 2013; Madiai *et al.*, 2016; Stamati *et al.*, 2016; Meza-Fajardo *et al.*, 2019). These studies suggest that 2D basin effects can have important implications for the earthquake-resistance design of new buildings and facilities, and for the safety evaluation of existing structures in areas located over alluvial valleys.

Starting in the 1970s, seismic building codes have included several provisions addressing the treatment of local site effects and the development of design ground motion. Currently, seismic codes exist and are enforced in many countries worldwide, with a total of 166 countries having codes in 2014 (Daniell *et al.*, 2014). Many current codes require design spectra to be obtained through site-specific ground response analysis or, for specific geometric and stratigraphic conditions, to account for 1D stratigraphic effects by means of code-based simplified approaches. Some codes [e.g. Eurocode 8 (CEN, 2004); Italian building code "Norme Tecniche per le Costruzioni" (MIT, 2018)] also provide a basic approach to account for topographic effects, while no building code or standard deals with site effects due to the subsurface geometry. Moreover, in current routine engineering practice, site specific design ground motions are usually developed by 1D analyses, neglecting multidimensional effects, possibly leading to non-conservative estimates of ground motion at sites in sedimentary basins. Because these unfavourable sites often pertain to highly populated areas, the availability of an expeditious though rational approach to predicting seismic ground response in such geological and geomorphological settings from the results of 1D response analysis or code-based spectra, is of prime interest to geotechnical engineers and engineering seismologists. Given the above, many researchers have tried to develop simplified methods to account for 2D/3D basin effects by means of a suitable 'aggravation factor' (Makra *et al.*, 2005; Paolucci and Morstabilini, 2006; Riga *et al.*, 2016; Madiai *et al.*, 2017; Zhu *et al.*, 2020). The aggravation factor (*AGF*) as defined by Chávez-García and Faccioli (2000) in terms of pseudo-acceleration spectral amplitudes, has proved to be a concise, efficient parameter for quantifying basin effects for design purposes. Therefore, it seems that such parameter could be reliably included in simplified approaches within seismic building code requirements.

This paper illustrates the main results and observations drawn from an initial investigation into 2D aggravation effects in symmetric basins overlain by two-layered deposits. More specifically, a preliminary investigation was conducted on *AGF* defined as the ratio between 2D and 1D pseudo-acceleration response spectra. To this end, a large number of 1D and 2D numerical linear visco-elastic local seismic response analyses were performed on simplified schemes approximating real sedimentary basins. The results described herein include: 1) the qualitative visual representation of the relationships between *AGFs* and a set of dimensionless parameters descriptive of basin geometry, stratigraphic layering, dynamic geotechnical soil properties, and seismic input motion; 2) the qualitative assessment of the relationship between peak aggravation values and corresponding spectral periods; and 3) the outcomes of a non-parametric statistical test aimed

at the quantitative assessment of the existence and strength of statistical dependency between the *AGF* and the aforementioned dimensionless parameters.

The distinctive features and main novelties of this research, with reference to available literature contributions, lie in: 1) the assignment of semi-sine-geometry to basin edges (arguably more realistic than the more frequently used trapezoidal-shaped edges); 2) the modelling of two-layered deposits (a condition that is often encountered in practice); 3) the use of an extended set of dimensionless parameters; and 4) the implementation of the non-parametric Kendall's tau test to assess statistical dependency.

2. Numerical modelling framework

The *AGF* defined by Chávez-García and Faccioli (2000) was used in this study to quantify the 2D basin effects from the outputs of 1D and 2D numerical analyses. Its mathematical expression is given by:

$$AGF(T,x) = \frac{S_{a,2D}(T,x)}{S_{a,1D}(T,x)} \tag{1}$$

where T is the spectral period, $S_{a,2D}(T, x)$ is the elastic pseudo-acceleration response spectrum for 5% damping ratio as obtained from two-dimensional analysis at a given control point located at a distance x from the centre of the basin surface, and $S_{a,1D}(T, x)$ is the response spectrum at the same control point from 1D analysis.

Response spectra for computing *AGF* using Eq. 1 were obtained by numerical ground response analysis performed using the Local Seismic Response-2D (LSR-2D) finite element software (STACEC, 2017). Symmetric two-layered basins were analysed, with soil 1 overlying soil 2. An elastic seismic bedrock was assumed, whose geometry can be fully described by the Bard and Bouchon (1980a) semi-sine-shaped formulation:

$$h(x) = H \qquad \text{for } |x| < L_i \tag{2a}$$

$$h(x) = \frac{H}{2}\left[1 + \cos\frac{\pi(x - L_i)}{L_o}\right] \qquad \text{for } L_i < |x| \le L_o + L_i \tag{2b}$$

$$h(x) = 0 \qquad \text{for } |x| > L_o + L_i \tag{2c}$$

where H is the maximum depth of the soil deposit at the centre of the basin; $2L_i$ is the inner width, i.e. the extension where depth has a constant H value; L_o is the outer width, i.e. the extension of basin edges. Based on these assumptions, $L = 2(L_i+L_o)$ is the total width of the basin. The general model geometry is shown in Fig. 1, where only the semi-width of the analysed model is represented.

Soil properties were assigned in terms of density, ρ, shear wave velocity, V_S, and Poisson's ratio, v, the latter allowing the calculation of compression wave velocity, V_P. The values assigned

to each of the two layers and to the underlying bedrock are given in Table 1.

Table 1 - Main properties of basin materials (V_S: shear wave velocity, ρ: density, G_0: small-strain shear modulus, D_0: small-strain damping ratio, v: Poisson coefficient).

Layer	V_S [m/s]	ρ [kg/m^3]	G_0 [MPa]	D_0 [%]	v [-]
Soil 1*	200; 300	1800	72; 162	1; 4	0.30; 0.35
Soil 2**	450; 600	2000	405; 720	1; 4	0.30; 0.35
Bedrock	800; 1100	2300	1472; 2783	0.05	0.15

* Top layer
** Bottom layer

A linear visco-elastic behaviour was hypothesised for bedrock and soil deposit, both assumed homogeneous, with shear modulus fixed at its small-strain value $G_0 = \rho \cdot V_S^2$, and damping ratio also assumed constant at its small-strain value D_0. The behaviour of the soils was assumed to be linear in order to make the 1D and 2D amplification functions, and consequently the *AGF*, only dependent on the geometry and material properties of the subsoil and independent of the amplitude of the input motion. The boundaries of the 2D models were fixed by extending the bedrock by a length $x_e = y_e = H$ both in the horizontal (on both sides of the basin) and vertical directions (Fig. 1). Normal and tangential viscous dampers were assumed at the boundary nodes to avoid wave reflection from the side boundaries within the analysis domain. Spectral *AGFs* were calculated at surficial control points evenly spaced at a constant horizontal spatial interval Δx = 50 m. The number of control points on the half-basin varies from 9 to 23, depending on the width of the cross-section scheme. 1D numerical analysis was performed on the associated soil profile located at each control point defined in the 2D model. To allow the comparison with the 2D analysis results independent of the software used, 1D ground response analyses were also performed by the code LSR-2D on the vertical stratigraphic profiles underlying each control point. A column of superimposed four-node rectangular elements was assumed to simulate 1D conditions. The two base nodes were assumed as transmitting nodes while all the other nodal points were only permitted to displace horizontally.

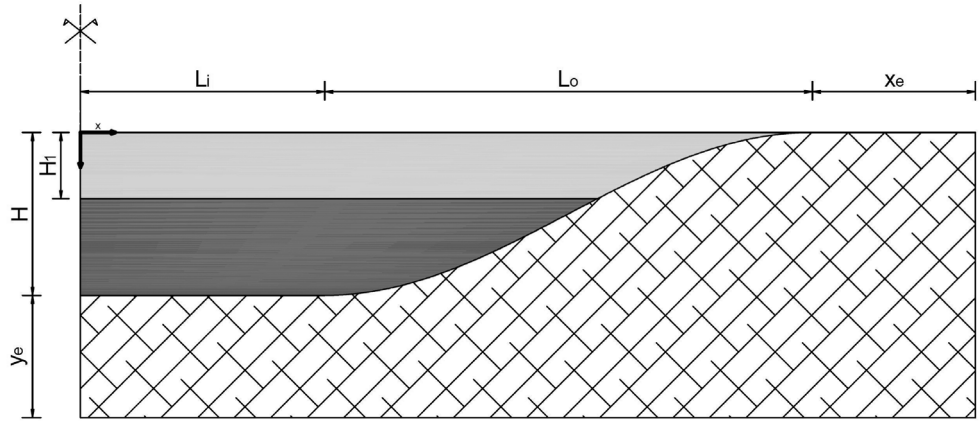

Fig. 1 - Half-width cross section scheme of the analysis models.

The 2D numerical analyses of the seismic response of all selected models, as well as the corresponding 1D analyses, were performed using Ricker Wavelet pulse (RW) acceleration time histories. The input motion was assumed as vertically propagating shear SH-waves and was simultaneously applied to all nodes at the base boundary of the analysis domain. It consisted of a single RW whose amplitude, in time and frequency domain, can be expressed by Eqs. 3 and 4, respectively:

$$A(t) = -\frac{\pi}{2}(a - 0.5)e^{-a} \tag{3}$$

$$F(f) = \frac{2}{\sqrt{\pi}}\frac{f^2}{{f_p}^3}e^{-\frac{f^2}{{f_p}^2}} \tag{4}$$

where $a = |\pi(t - t_s)f_p|^2$; t_s is the time from the start of motion corresponding to the occurrence of peak acceleration, and f_p is the predominant frequency. RW were selected as their shape (pulse) and frequency content (narrow band) have been found to enhance the influence of some aspects of the seismic excitation (i.e. the predominant frequency) over other aspects (i.e. duration, amplitude, irregularity of time history) that may have little significance if linear visco-elastic analyses are performed. Three predominant frequency values (f_p = 0.6 Hz, 2 Hz, and 10 Hz) were considered in this study. A peak acceleration *PGA* = 0.79 g was set to occur at t_s = 3 s for all frequencies. Because a linear visco-elastic soil behaviour is assumed, the results obtained can be considered independent of the amplitude of the input signal. For this reason, only one *PGA* value of the input motion was used to perform the analysis. The set of predominant frequencies considered in the studies spans over typical relevant ranges reflecting real seismic events. Fig. 2 shows the acceleration time history and the Fourier spectrum for the input motion consisting in the Ricker wavelet having the intermediate frequency of 2 Hz.

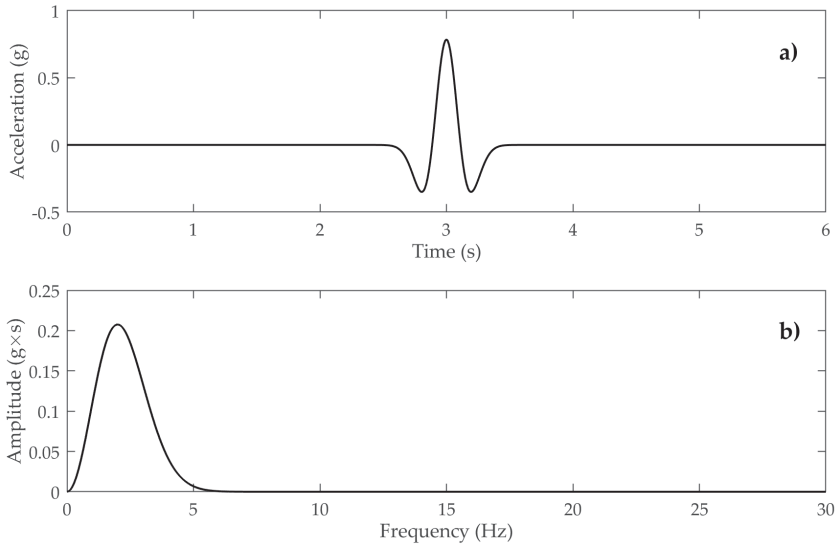

Fig. 2 - Ricker wavelet pulse (Eqs. 3 and 4) with t_s = 3 s and f_p = 2 Hz, in the: a) time domain; and b) frequency domain.

A total of 192 2D basin models were obtained by combining the different physical and mechanical parameters reported in Table 1, that characterise the two soil layers, with the geometrical parameters reported in Table 2 (L_o, L_i, H), that identify the type sections. A number of models, which were deemed physically non-realistic, were excluded *a priori* from all possible combinations generated before performing the analyses. Results of 1D and 2D ground response were collected in the form of pseudo-acceleration elastic response spectra (5% damping ratio) for periods ranging from 0 to 4 s with a spectral period step ΔT = 0.01 s**.** Peak values of spectral AGF_{max} were retrieved for each control point in each of the 192 models, along with the corresponding spectral period, termed fundamental aggravation period T_f.

Table 2 - Geometric and dimensionless parameters for the different sections' shapes.

Section shape	L_o [m]	L_i [m]	H [m]	k_{HL} [-]	k_{Hint} [-]	k_{xL} (L_i)[-]
1 (2)	250	150	50	0.125	0.25 (0.50)	0.375
3 (4)	250	300	100	0.182	0.25 (0.50)	0.545
5 (6)	500	300	100	0.125	0.25 (0.50)	0.375
7 (8)	500	600	200	0.182	0.25 (0.50)	0.545

3. Model parameterisation

Calculated values of peak spectral aggravation ranged from 0.65 to 1.95, with fundamental aggravation periods spanning the full range of possible spectral periods considered in the analysis. The significant scatter in AGF_{max} and T_f attests to the complexity and heterogeneity of 2D aggravation phenomena. To attempt an initial comprehension of causal relationships between dimensional, geometric, geotechnical, and seismic loading attributes of the respective modelling schemes and aggravation phenomena, AGF_{max} outputs were investigated with respect to such attributes. In most available literature contributions, investigations on *AGFs* are structured, performed, and reported in terms of site-specific conditions. Some studies, however, refer to dimensionless parameters (Bard and Bouchon, 1980a, 1980b, 1985; Bouckovalas and Papadimitriou, 2005; Vessia and Russo, 2013; Pitilakis *et al.*, 2015; Riga *et al.*, 2016, 2018; Zhu and Thambiratnam, 2016; Zhu *et al.*, 2018a, 2018b, 2020; Alleanza *et al.*, 2019; Papadimitriou, 2019; Ayoubi *et al.*, 2021) as this facilitates the generalisation of findings to an extended range of schemes beyond those used in the source analyses. The latter approach is adopted in this study by defining a set of dimensionless parameters, which can adequately and efficiently parameterise the geometric, geotechnical, and seismic properties of the aforementioned 2D and 1D models as described in the following.

The width-normalised distance (e.g. Bard and Bouchon, 1985) describes the spatial location of control points with respect to basin width:

$$k_{xL} = \frac{x}{L_i + L_o} \tag{5}$$

The shape ratio (e.g. Bard and Bouchon, 1980a, 1985; Bouckovalas and Papadimitriou, 2005) is the ratio of maximum thickness of the basin to its half-width:

$$k_{HL} = \frac{H}{L_i + L_o} \tag{6}$$

The normalised depth of the interface, with respect to the maximum thickness of the basin, is:

$$k_{Hint} = \frac{H_1}{H} \tag{7}$$

The seismic impedance ratios between the bedrock and each soil layer (Eqs. 8 and 9), and between the two covering soil layers (Eq. 10) were considered:

$$k_{Ibs\mathbf{1}} = \frac{V_{Sb}}{V_{Ss1}} \cdot \frac{\rho_b}{\rho_{s1}} \tag{8}$$

$$k_{Ibs2} = \frac{V_{Sb}}{V_{Ss2}} \cdot \frac{\rho_b}{\rho_{s2}} \tag{9}$$

$$k_{Is2s1} = \frac{V_{Ss2}}{V_{Ss1}} \cdot \frac{\rho_{s2}}{\rho_{s1}} \tag{10}$$

where the subscripts *b*, *s*1, and *s*2 refer here and hereinafter to bedrock, soil 1, and soil 2, respectively.

The dimensionless wavelength-normalised height, modified from the single-layer case proposed by Bouckovalas and Papadimitriou (2005) was used to combine basin geometry, dynamic geotechnical properties of the deposit, and seismic input characteristics. It is defined as:

$$k_{H\lambda} = \frac{H}{\lambda_{s,eq}} \tag{11}$$

where

$$\lambda_{s,eq} = V_{Ss,eq}/f \tag{12}$$

is the equivalent wavelength of the vertically propagating SV-waves.

In the previous equation, $V_{Ss,eq}$ is the equivalent shear wave velocity of the deposit calculated at the basin centre according to:

$$V_{Ss,eq} = (V_{Ss1}.H_1 + V_{Ss2}.H_2)/H \tag{13}$$

The dimensionless wavelength-normalised basin width at the surface is also introduced as:

$$k_{L\lambda} = \frac{L_o + L_i}{\lambda_{s1}} \tag{14}$$

where it is assumed that the wavelength of the surface waves propagating horizontally in the top layer is equal to the shear wave velocity in the same layer, i.e. $\lambda_{s1} = V_{Ss}1/f$.

Two further parameters were defined as the ratio of damping ratio values (Eq. 15) and of Poisson coefficient values (Eq. 16) of the top and bottom soil layer:

$$k_{Ds} = \frac{D_{s1}}{D_{s2}} \tag{15}$$

$$k_{\nu s} = \frac{\nu_{s1}}{\nu_{s2}} \tag{16}$$

Furthermore, to assess the effect of model size and geometry, models were classified into 8 section shapes based on combinations of L_o, L_i, and H as given in Table 2. The thickness of the upper layer in the odd-number sections is half that in the even-number sections (one quarter and one half of the total thickness of the deposit in the centre of the basin, respectively); moreover, considering the odd and even sections separately, width and depth increase as the section number increases. The ratio L_i/L_o in sections 1, 2, 5, 6 is half of that in sections 3, 4, 7, 8, so that the basin sides extend from $k_{xL} > 0.375$ and $k_{xL} > 0.545$, respectively.

The whole set of values taken by dimensionless parameters k_{xL}, k_{HL}, k_{Hint}, k_{lbs1}, k_{lbs2}, k_{ls2s1}, $k_{H\lambda}$, $k_{L\lambda}$, k_{Ds}, and k_{vs} is given in Table 3.

Table 3 - Ranges of dimensionless parameters.

Parameter	Values
k_{xL}	[0.00, 0.04, 0.06, 0.09, 0.12, 0.14, 0.18, 0.19, 0.23, 0.25, 0.27, 0.31, 0.32, 0.36, 0.38, 0.41, 0.44, 0.46, 0.50, 0.55, 0.56, 0.59, 0.62, 0.64, 0.68, 0.69, 0.73, 0.75, 0.77, 0.81, 0.82, 0.86, 0.88, 0.91, 0.92, 0.94, 0.96, 0.97, 1.00]
k_{HL}	[0.125, 0.182]
k_{Hint}	[0.25, 0.50]
k_{lbs1}	[3.41, 4.68, 5.11, 7.03]
k_{lbs2}	[1.53, 2.04, 2.11, 2.81]
k_{ls2s1}	[1.67, 2.22, 2.50, 3.33]
$k_{H\lambda}$	[0.057, 0.060, 0.067, 0.073, 0.077, 0.080, 0.114, 0.120, 0.133, 0.145, 0.155, 0.160, 0.190, 0.200, 0.222, 0.229, 0.240, 0.242, 0.258, 0.267, 0.291, 0.310, 0.320, 0.381, 0.400, 0.444, 0.485, 0.516, 0.533, 0.762, 0.800, 0.889, 0.952, 0.970, 1.000, 1.032, 1.067, 1.111, 1.212, 1.290, 1.333, 1.905, 2.000, 2.222, 2.424, 2.581, 2.667, 3.810, 4.000, 4.444, 4.848, 5.161, 5.333]
$k_{L\lambda}$	[0.80, 1.10, 1.20, 1.60, 1.65, 2.20, 2.40, 2.67, 3.30, 3.67, 4.00, 5.33, 5.50, 7.33, 8.00, 11.00, 13.33, 18.33, 20.00, 26.67, 27.50, 36.67, 40.00, 55.00]
k_{Ds}	[0.25, 4.00]
k_{vs}	[0.86, 1.17]

It is worth noting that while some of the above dimensionless parameters are taken from the literature (albeit using different notations), others are introduced here specifically for two-layered basins. The breadth and comprehensiveness of the set of dimensionless parameters provide one of the novel elements of this paper.

4. Investigation into aggravation phenomena

The numerous models, control points and dimensionless parameters, result in a large data set of dimensionless parameters and *AGFs*. Such data set is affected by significant scatter in both input and output parameters. Variability in output aggravation values can be ascribed to multiple sources; namely: 1) aleatory uncertainty in peak *AGFs* stemming from the 'real' variability in the level of aggravation for different basin models and seismic inputs; and 2) model uncertainty stemming from the approximation of the complex physical phenomena between propagating waves and the soil-bedrock system, which is inherent in numerical analyses. While the first cannot be reduced artificially, the second can in principle be reduced by refining the numerical modelling process. While the ultimate goal of the broader ongoing research is the implementation of 2D basin effects in seismic design codes, this paper focuses solely on a preliminary analysis of the data, where 'preliminary' refers to subsequent step of the overall process, which will be the object of future research. This section describes the preliminary qualitative and quantitative analyses conducted on the aggravation data set. However distant the outputs of these analyses may lie from the terminal stages of the research, they are important as they allow: 1) assessing the level of variability in peak aggravation values; 2) understanding the distribution of *AGFs* with respect to fundamental aggravation periods; 3) identifying which dimensionless parameters, among those listed in Table 3, display the strongest correlation with the *AGF* and defining an 'optimal' set of dimensionless parameters for future operations; and 4) identifying possible outliers and planning for dedicated analyses aimed at assessing their causes.

Though the number of analysed models is considerably high with respect to most previous research contributions, an exhaustive investigation into causal relationships would require a significantly more numerous source data set. The observations and assessments provided in the following sections refer specifically to the data available so far and do not aim to provide general statements and inferences.

4.1. Qualitative analysis

The first mode of investigation in this study consists in the qualitative, visual inspection of scatterplots of peak aggravation values with respect to: 1) the corresponding fundamental aggravation periods; and 2) the dimensionless parameters k_{xL}, k_{HL}, k_{Hint}, k_{Ibs1}, k_{Ibs2}, k_{Is2s1}, $k_{H\lambda}$, $k_{L\lambda}$, k_{Ds}, and k_{vs}. In general terms, the visual inspection of scatterplots is useful to detect trends and possible outliers to these trends, and to set the bases of subsequent analyses involving, for instance, the selection of analytical models to be applied to the data. Each point in the scatterplots shown in Figs. 3 to 11 refers to a specific model and to a specific control point. Fig. 3 plots AGF_{max} values versus the fundamental aggravation periods by section shape. Examination of Fig. 3 reveals that highest values of AGF_{max} (>1.7) occur for shapes 2 to 6 while shapes 1, 7, and 8 present lower peak values (<1.7). All section shapes with the exception of shape 8 display the highest values of peak spectral aggravation for T_f < 0.8 s. Shape 8 displays lower values of AGF_{max} for T_f < 1.0 s but higher values for T_f > 1.0 s with respect to other shapes. No cases of AGF_{max} > 1.1 are observed

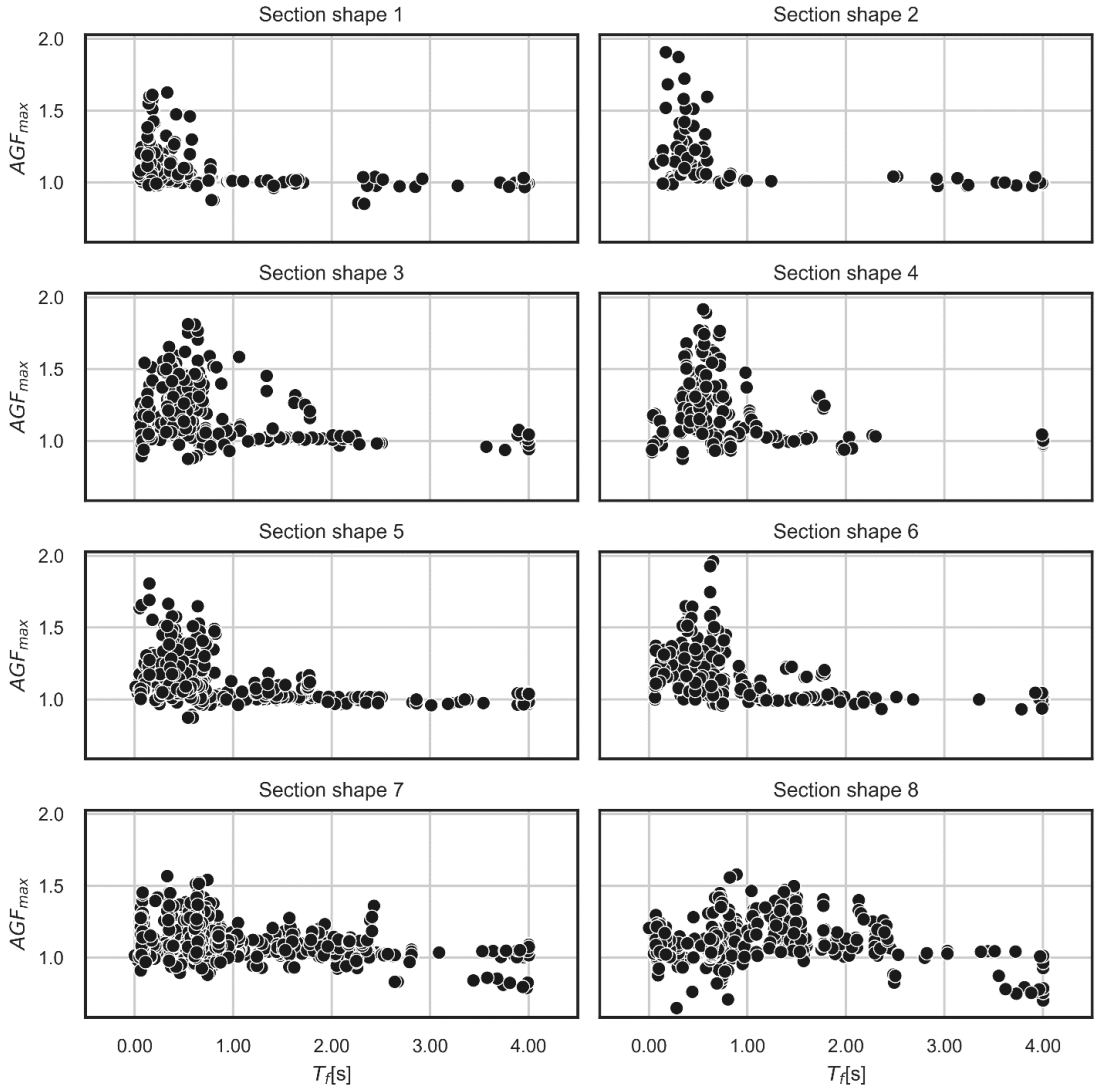

Fig. 3 - Scatterplot of fundamental aggravation periods versus AGF_{max} by section shape.

for $T_f > 2.4$ s for any shape. A reduction of 2D pseudo-acceleration response spectrum amplitude with respect to 1D conditions (i.e. $AGF_{max} < 1.0$) is observed for all shapes and for the full range of the considered spectral periods; however, the lowest values of AGF_{max} pertain to section shapes 7 and 8, i.e. to larger basins.

Fig. 4 plots the values of AGF_{max} versus the fundamental aggravation periods (normalised by the fundamental period of the associated 1D soil column, T_{f1D}) by section shape. Normalisation by T_{f1D} allows the assessment of the existence and relevance of the effect of the variation in fundamental period from the 1D and 2D schemes on the magnitude of aggravation phenomena. Visual inspection of Fig. 4 reveals that the range of T_f/T_{f1D} decreases progressively from shape 1 (which displays maximum values of 10.5) to shape 8 (with maxima around 2.5). For all section shapes, highest values of AGF_{max} correspond to $T_f/T_{f1D} < 1$. Values of AGF_{max} are lower than 1.1 for $T_f/T_{f1D} > 2$ for all shapes.

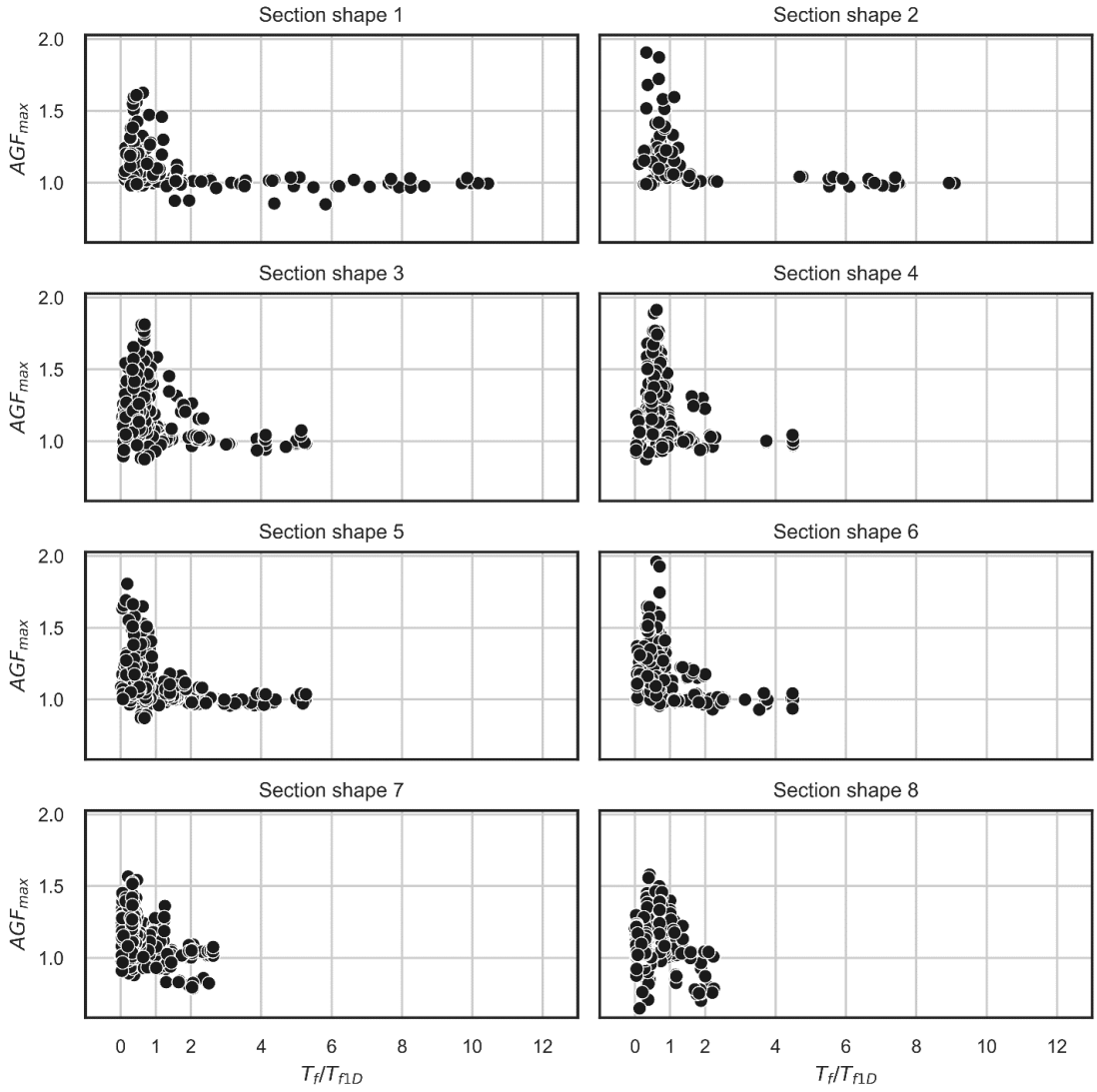

Fig. 4 - Scatterplot of fundamental aggravation periods (normalised by the fundamental period of the associated 1D soil column, T_{f1D}) versus AGF_{max} by section shape.

Fig. 5 plots the fundamental aggravation periods (multiplied by the predominant frequency of the input Ricker wave, f_p, which is equivalent to normalisation by the predominant period of the same input motion) versus AGF_{max} by section shape. Such normalisation allows the assessment of the relationship between amplification phenomena induced by quasi-resonance conditions in damped systems and 2D aggravation effects. The range of $T_f \cdot f_p$ spans from values just over 0 to approximately 8 for shapes 1 to 6, while shape 7 presents a cluster of points between 8 and 9 and shape 8 displays a single point at 9.7. No significant trends in AGF_{max} with respect to $T_f \cdot f_p$ are evident for any shape though highest values of AGF_{max} occur for $0.5 < T_f \cdot f_p < 6$. Lower values of AGF_{max} also occur for a wide range of values of $T_f \cdot f_p$.

Figs. 6, 7, 8, 9, 10, and 11 plot peak *AGFs* versus the dimensionless parameters k_{xL}, k_{lbs1}, k_{lbs2}, k_{ls2s1}, and $k_{H\lambda}$, and $k_{L\lambda}$, respectively, by section shape. Outputs are shown for this subset of dimensionless parameters since the others take only one (i.e. k_{HL}, k_{Hint}) or two (i.e. k_{Ds}, k_{vs}) values

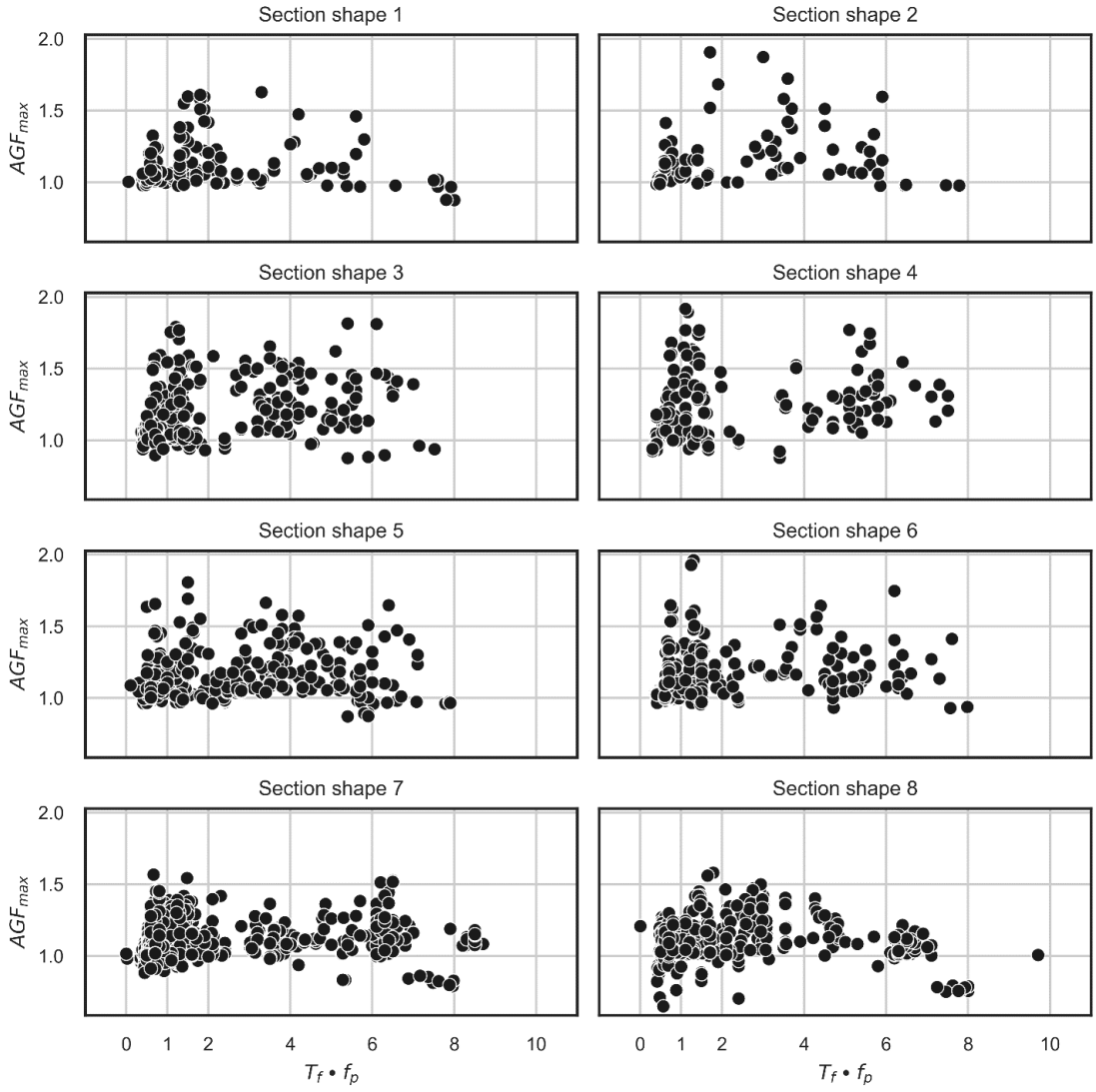

Fig. 5 - Scatterplot of fundamental aggravation periods (normalised by the fundamental period of the input Ricker wave) versus AGF_{max} by section shape.

per section shape and since no significant trends are detected. This paper does not present detailed descriptive statistics (i.e. mean, standard deviation, etc.) of peak aggravation in relation to the values of dimensionless parameters as the focus is on the preliminary identification of the most relevant factors in terms of causal relationships with 2D basin aggravation effects. Fig. 6 allows the appreciation of spatial variability of AGF_{max} along the surface of the basin. A general pattern can be observed for all section shapes, whereby high values of AGF_{max} occurring at the centre of the basin. Aggravation values then decrease progressively in the range $0 < k_{xL} < 0.20$, to increase again until local maxima are attained for different values of k_{xL} (ranging from 0.40 to 0.60) in different section shapes. Following this local maximum, a progressive decrease in AGF_{max} is noted for all shapes except for shape 7, which shows an additional local maximum around $k_{xL} = 0.70$. Significant de-aggravation effects (i.e. $AGF_{max} < 0.9$) occur only for $k_{xL} > 0.60$. A cluster of possible outliers is detected for $k_{xL} \approx 0.80$ for section shape 5. Further investigations are required

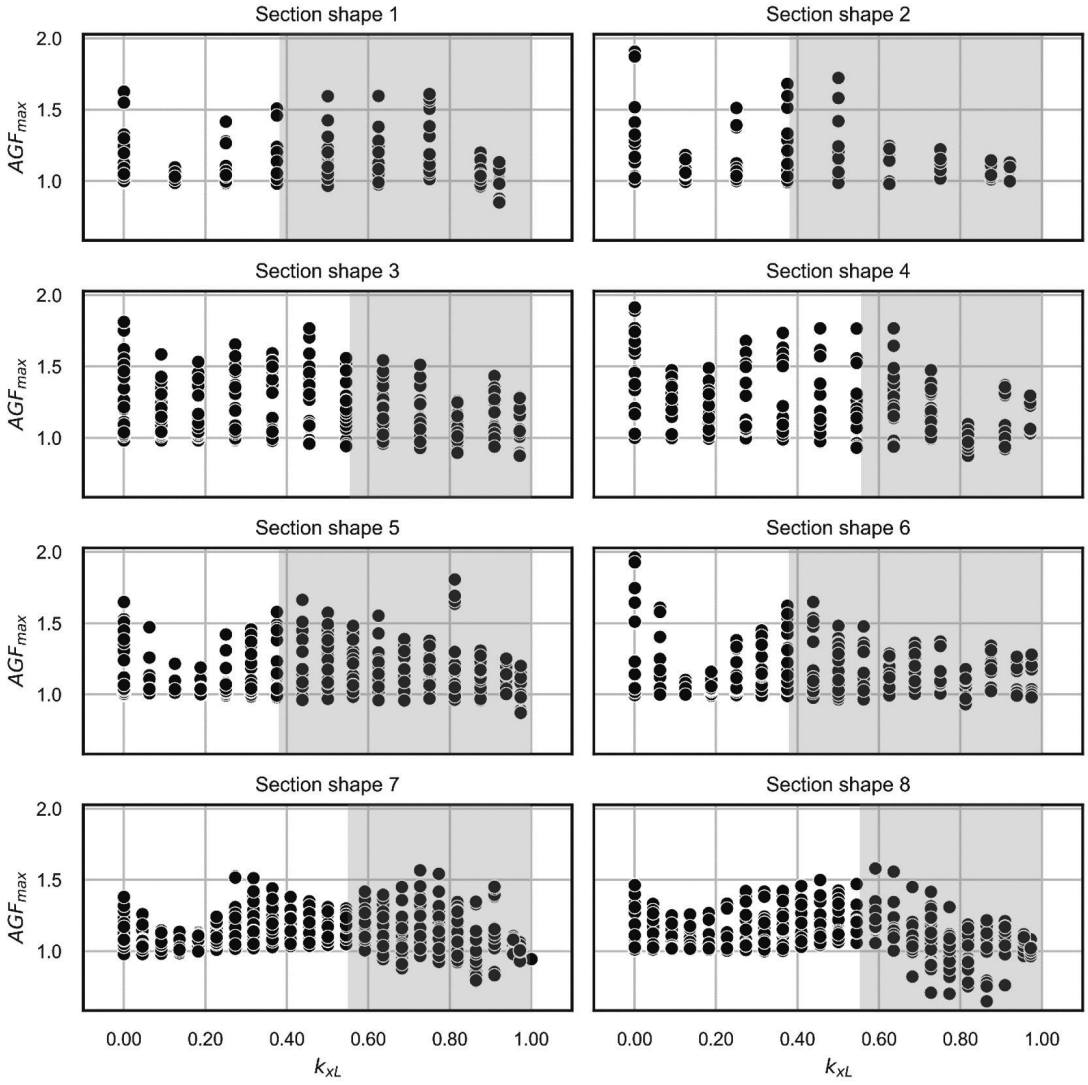

Fig. 6 - Scatterplot of k_{xL} versus AGF_{max} by section shape (the spatial extensions corresponding to basin sides are shaded in gray).

to establish whether this cluster stems from the numerical modelling process or from 'real' phenomena determining a distinct level of aggravation with respect to adjacent data points.

Fig. 7 suggests an overall tendential increase in the scatter of AGF_{max} with increasing values of k_{lbs1} though this trend is not univocally identified in all section shapes (see for instance shapes 3, 7, and 8). The interpretation of AGF_{max} with respect to k_{lbs1} in section shapes 2, 4, 6, and 8 is difficult because the former takes only two values in these cases. The same overall trends can be identified for k_{lbs2} (Fig. 8). Fig. 9 suggests a less definite trend, with larger scatter in AGF_{max} occurring for lower and higher values of k_{ls2s1} and lower scatter observed for intermediate values for shapes 1, 3, 5, and 7 for which 3 values of k_{ls2s1} are available. Fig. 10 reveals that low values of $k_{H\lambda}$ correspond to low values and small scatter in AGF_{max} for all section shapes, with shapes 7 and 8 displaying the most significant de-aggravation scenarios for $k_{H\lambda} < 1$. No significant trends in AGF_{max} are apparent, possibly with the exception of the small scatter and absence of values of

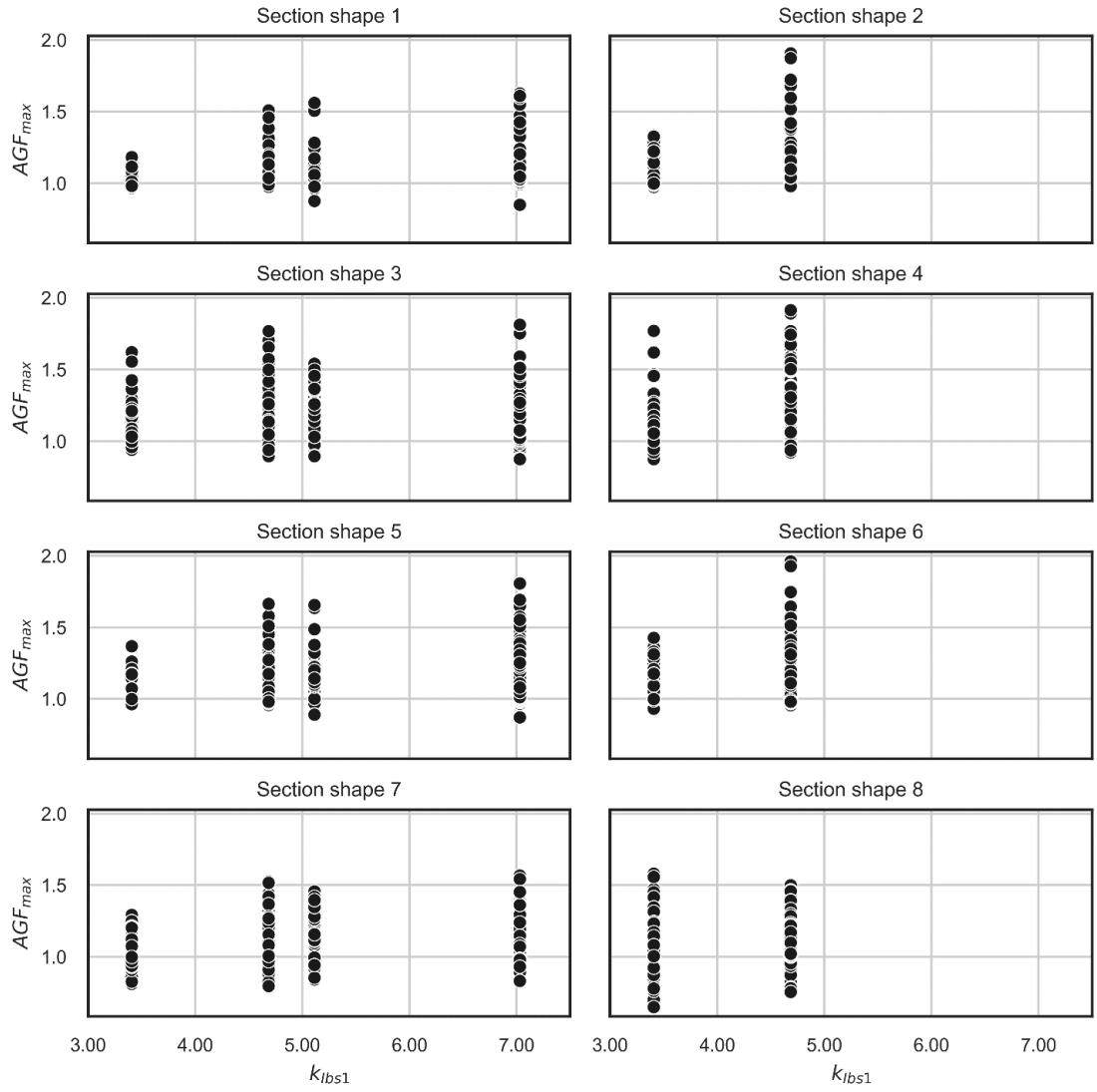

Fig. 7 - Scatterplot of k_{lbs1} versus AGF_{max} by section shape.

AGF_{max}> 1.5 noted for $k_{H\lambda}$ > 3 in shapes 7 and 8. The interpretation of the causality between $k_{L\lambda}$ and AGF_{max} shown in Fig. 11 is difficult because significantly distinct behaviours are observed for different section shapes. For instance, shapes 1, 2, and 5 display increasing upper-bound values and scatters in AGF_{max} with increasing $k_{L\lambda}$ while shapes 3, 4, and 6 seem to present the inverse behaviour. A less monotonic behaviour is observed for shapes 7 and 8, with initial increases in the scatter and in upper-bound values and decreases in lower-bound values of AGF_{max} for increases of $k_{L\lambda}$ up to approximately 10, and subsequent inversion of this behaviour. A common trait to all section shapes lies in the small scatter and low aggravation values noted for $k_{L\lambda}$ < 2.

4.2. Quantitative analysis

The quantitative approach to the preliminary investigation on 2D aggravation outputs is aimed at assessing the existence and relevance of well-defined relationships between *AGFs* and

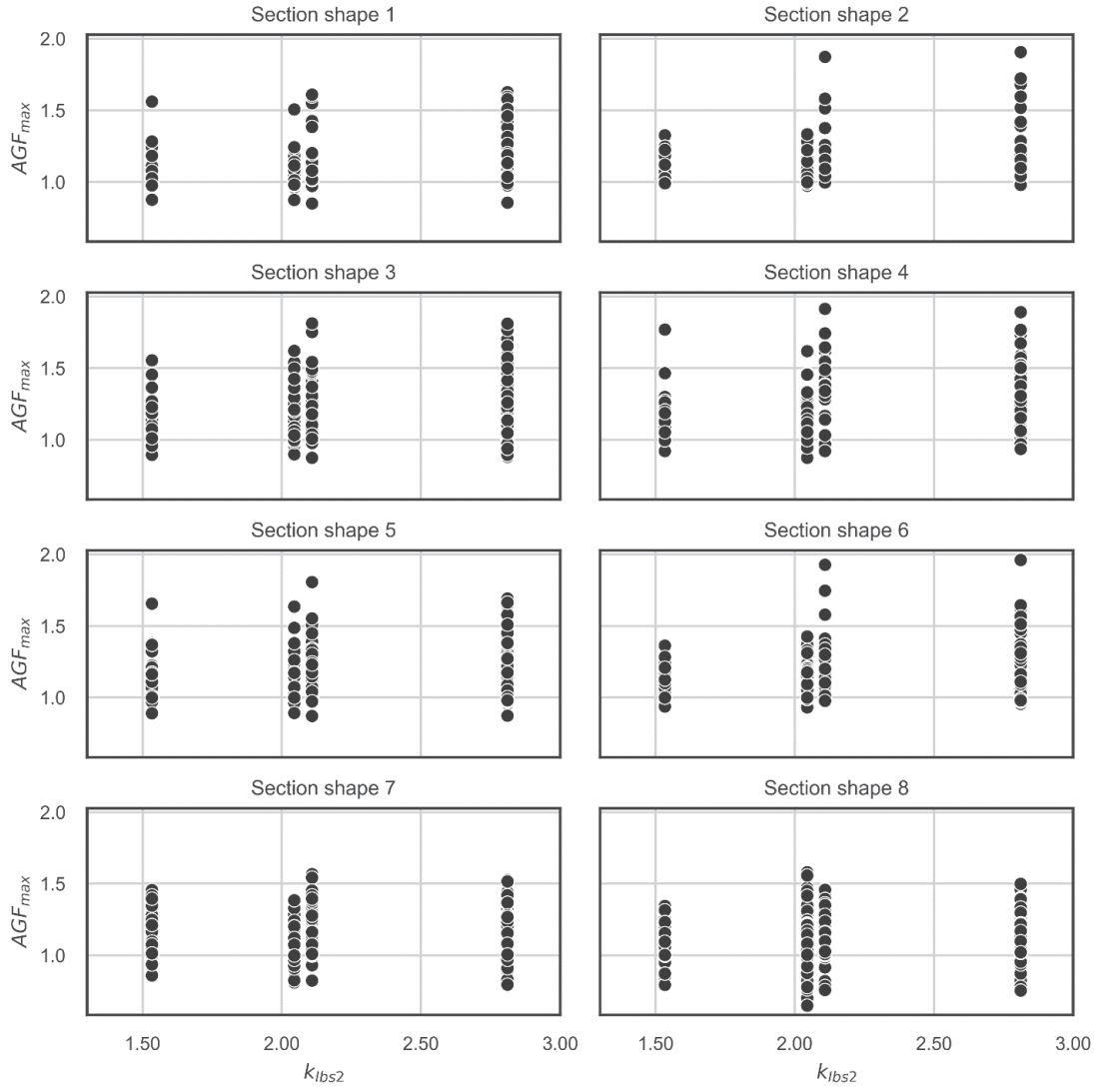

Fig. 8 - Scatterplot of k_{lbs1} versus AGF_{max} by section shape.

the reference dimensionless parameters k_{xL}, k_{HL}, k_{Hint}, k_{lbs1}, k_{lbs2}, k_{ls2s1}, $k_{H\lambda}$, $k_{L\lambda}$, k_{Ds}, and k_{vs}. Such effort relies on the assessment of statistical dependency and it is conducted through Kendall's tau test (Daniel, 1990), a non-parametric statistical test, which has been frequently used for geotechnical applications (Uzielli *et al.*, 2019). Kendall's test involves the calculation of Kendall's tau, τ_{ken}, which measures the probability of concordance minus the probability of discordance among measurements in a data set. The test statistic is given by:

$$\tau_{ken} = \frac{n_c - n_d}{\frac{1}{2}N(N-1)} \tag{17}$$

where N is the number of pairs of observations in a data set, n_c is the number of concordant pairs of observations and n_d is the number of discordant pairs. A pair of observations (x_i, y_i),

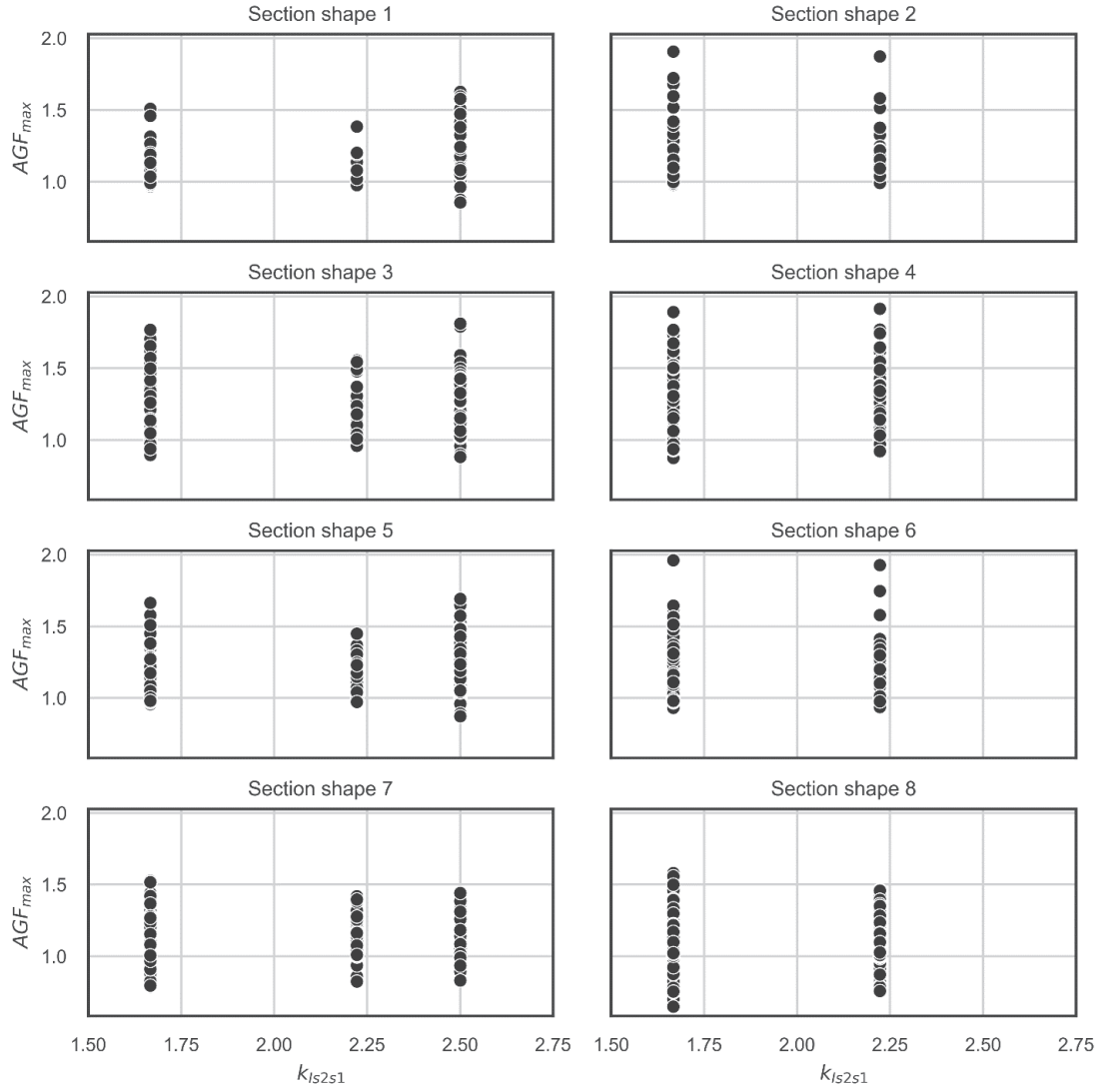

Fig. 9 - Scatterplot of k_{ls2s1} versus AGF_{max} by section shape.

(x_j, y_j) is said to be concordant if $x_i > y_i$ and $x_j > y_j$, while it is said to be discordant if $x_i > x_j$ and $y_i < y_j$. The calculation of τ_{ken} relies on a total of (1/2) $N(N\text{-}1)$ comparisons between all possible pairs of observations. Possible values of τ_{ken} range from -1 to +1, indicating, respectively, perfect negative and positive correlation (in both cases, a strong statistical dependency, that is, a strong correlation). A value close to zero indicates absence of statistical dependency (i.e. no correlation).

To assess statistical dependence at a given significance level, the following statistic can be calculated:

$$z_{ken} = \frac{3(n_c - n_d)}{\sqrt{N(N-1)(2N+5)/2}} \tag{18}$$

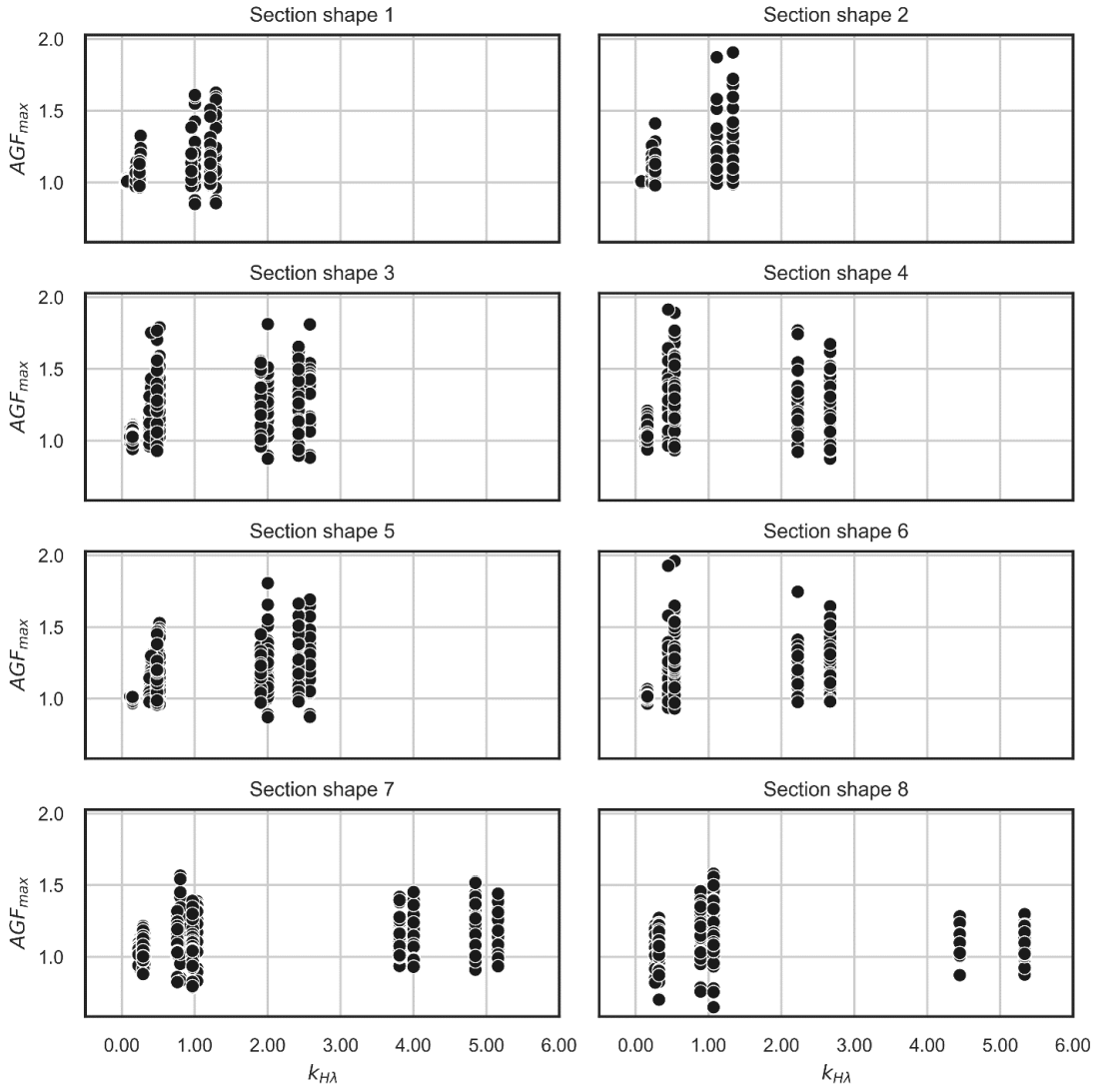

Fig. 10 - Scatterplot of $k_{H\lambda}$ versus AGF_{max} by section shape.

The statistic z_{ken} is distributed approximately as a standard normal in case of statistical independence. For a two-tailed test, the ρ-value can thus be calculated as twice the cumulative probability for a standard normal at $-|z_{ken}|$. If the calculated ρ-value is below the given significance level, the null hypothesis at that significance level that the variables are statistically independent is rejected. Table 4 reports the outputs of Kendall's tau test for the relationship between a subset of the dimensionless parameters and AGF_{max}. Calculated values of τ_{ken} are tabulated for each parameter along with the assessment of statistical dependence (Yes/No) at a significance level of 0.05. Outputs are provided for both by section shape and for the aggregate data set (i.e. for all section shapes jointly). Inspection of Table 4 attests to the inter-parameter and inter-section heterogeneity of statistical dependence. For k_{xL}, for instance, statistical dependency is assessed at aggregate level and, at section shape-level, section shapes 3, 4, and 8, while no significant correlation is assessed for shapes 1, 2, 5, 6, and 7. The sign of τ_{ken} also varies among shapes, indicating

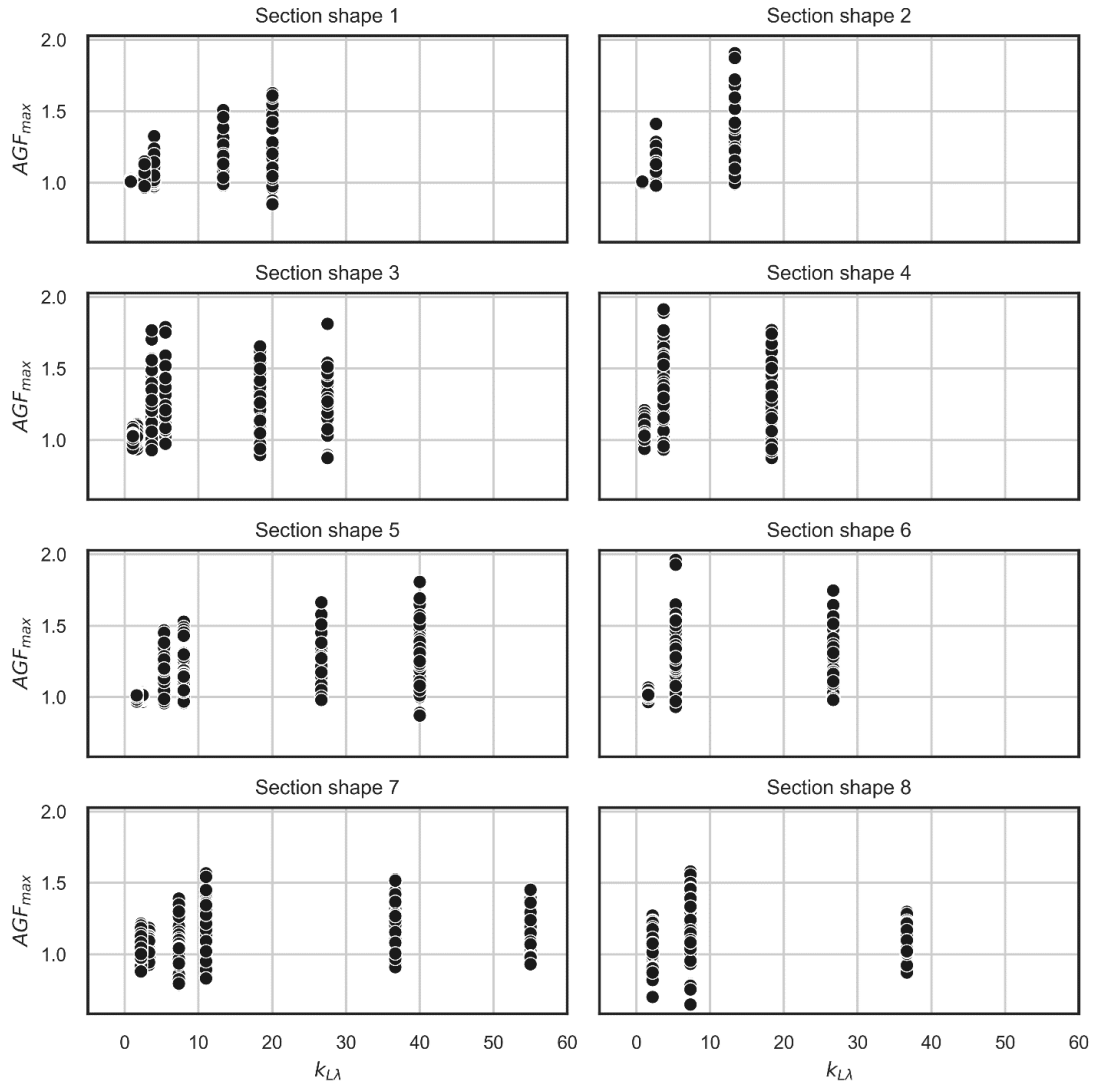

Fig. 11 - Scatterplot of $k_{L\lambda}$ versus AGF_{max} by section shape.

the alternance between direct and inverse correlation. The parameters k_{lbs1} and k_{lbs1} show almost uniformly a significant direct correlation with AGF_{max} with the sole exception of k_{lbs1} for section shape 1. Conversely, k_{vs}, k_{Ds}, and k_{ls2s1} never display significant correlation with AGF_{max} at aggregate or shape-specific level. Lastly, $k_{H\lambda}$ and $k_{H\lambda}$ are statistically significantly and directly correlated with AGF_{max} at aggregate level and for section shapes 1 to 7 while no significant correlation is assessed for shape 8 for either parameter. Kendall's tau test cannot be applied at individual-section shape level for k_{HL} and k_{Hint} because these parameters take only one value per section shape.

The outputs of Kendall's tau test are useful in supplementing the qualitative assessments deriving from the visual inspection while providing more objective statistical criteria for assessing the influence of each of the dimensionless parameters on 2D aggravation effects for each section shape. However, Kendall's tau test does not allow some important observations, which could be inferred from visual inspection, such as the pattern of spatial variation of peak aggravation as represented in Fig. 6.

Table 4 - Outputs of Kendall's tau test for dimensionless parameters and assessment of statistical dependency of peak spectral *AGF*.

Section		k_{xL}	k_{HL}	k_{vs}	k_{Ds}	k_{Ibs1}	k_{Ibs2}	k_{Is2s1}	k_{Hint}	$k_{H\lambda}$	$k_{L\lambda}$
All	τ_{ken}	-0.063	0.123	0.016	-0.016	0.096	0.133	-0.003	0.048	0.311	0.295
	dep.	Y	Y	N	N	Y	Y	N	Y	Y	Y
1	τ_{ken}	0.076	-	0	0	0.087	0.139	-0.005	-	0.416	0.427
	dep.	N	-	N	N	N	Y	N	-	Y	Y
2	τ_{ken}	0.014	-	-0.031	-0.031	0.182	0.15	-0.004	-	0.503	0.561
	dep.	N	-	N	N	Y	Y	N	-	Y	Y
3	τ_{ken}	-0.135	-	-0.026	-0.026	0.162	0.171	0.054	-	0.412	0.418
	dep.	Y	-	N	N	Y	Y	N	-	Y	Y
4	τ_{ken}	-0.211	-	-0.04	-0.04	0.183	0.166	-0.029	-	0.296	0.317
	dep.	Y	-	N	N	Y	Y	N	-	Y	Y
5	τ_{ken}	0.003	-	-0.02	-0.02	0.135	0.142	0.044	-	0.475	0.479
	dep.	N	-	N	N	Y	Y	N	-	Y	Y
6	τ_{ken}	-0.05	-	-0.052	-0.052	0.185	0.156	0	-	0.364	0.397
	dep.	N	-	N	N	Y	Y	N	-	Y	Y
7	τ_{ken}	-0.049	-	-0.011	-0.011	0.082	0.131	-0.004	-	0.208	0.2
	dep.	N	-	N	N	Y	Y	N	-	Y	Y
8	τ_{ken}	-0.102	-	-0.022	-0.022	0.104	0.102	-0.044	-	-0.027	-0.051
	dep.	Y	-	N	N	Y	Y	N	-	N	N

5. Concluding remarks and future developments

Seismic ground response analyses were performed on a large number of models to evaluate 2D aggravation effects in symmetric basins overlain by two-layered soil deposits. A wide range of dimensional, geometric, geotechnical, and seismic loading properties were considered to assess preliminarily and at a descriptive level the variability and causality of aggravation effects response to a number of dimensionless parameters related to basin size and geometry, dynamic geotechnical properties of the soil deposits, and characteristics of the input motion. Basin-induced aggravation effects were quantified by means of the peak value AGF_{max} of the spectral *AGF*, the latter having been defined as the ratio between 2D and 1D acceleration response spectra along the basin surface.

The paper illustrated a set of qualitative and quantitative analyses focusing on: a) the relationship between peak spectral aggravation and the spectral period of occurrence; and b) the relationship between AGF_{max} and a large set of dimensionless parameters, which parameterise the modelled basins and seismic inputs. The analyses are intended to be preliminary to subsequent investigations ultimately aimed at the definition of a procedure for the inclusion of basin effects in seismic design codes. The following main conclusions can be drawn from the results:

- spectral aggravation values are markedly variable spatially along the basin surface for all geometries, geotechnical conditions, and seismic inputs;
- the set of dimensionless parameters adopted in the study herein provides a good starting point for the definition of a restricted set of parameters to be related to spectral aggravation outputs following the conduction of further studies;
- for shallow- to medium-depth basin models, values of peak spectral aggravation are higher

and fundamental aggravation periods are longer than for deeper-depth models;
- over the flat parts of the basins, peak spectral aggravation increases with shape ratio and normalised interface depth, especially in the central part of the basins;
- at the far end basin sides and near basin edges, peak spectral aggravation values are only slightly higher or in some case even lower, than unity. This is especially true for deeper-thickness models, meaning that 2D effects in these portions of the basins are moderate or beneficial with respect to the corresponding 1D response;
- the existence and strength of causal relationships between dimensionless parameters and peak spectral aggravation values (as assessed through visual inspection and statistical dependence testing at a significance level 0.05) is evident for 6 out of the 10 dimensionless parameters considered in the study, though the dependence from spatial location along the surface is not statistically significant for all section shapes.

The qualitative and quantitative assessments provide useful complementary indications for the preliminary assessment of the outputs of the numerical analyses. A main goal of the preliminary analysis is the identification of several issues requiring scrutiny in further studies. First, some of the dimensionless parameters are sparse, i.e. their values are either not sufficient in number or evenly spaced to allow more robust assessment of their relationship with *AGFs*. Future investigations should rely on additional models opportunely defined as to ensure sufficient regularity in the dimensionless parameters defined herein. Second, a few potential outliers were detected and require dedicated investigations to establish the cause for their discontinuity with respect to the main cloud of data points, i.e. whether the local variability in outputs reflects a 'real' aleatory uncertainty or whether numerical modelling approximations induce epistemic uncertainty into the output data set. The observations and conclusions drawn herein may be verified, confirmed, and generalised through future investigations relying on a more robust data set.

Overall, the investigations conducted so far are very encouraging in that they effectively allow the preliminary identification of a set of dimensionless parameters, which display statistically significant correlation with *AGFs*. Moreover, for some of the parameters it is possible to identify well-defined correlations with *AGFs*, including the general trend of spatial variability of aggravation. The integration between qualitative and quantitative assessments proves to be effective and to enhance the preliminary interpretation of outputs as performed herein.

Acknowledgments. This study was partially supported by DPC-ReLUIS Research Project 2019-2021. An extended summary and an oral communication pertaining to this study were presented at the 39th GNGTS Online Conference held on June 22-24, 2021.

REFERENCES

Alleanza G.A., D'Onofrio A., Silvestri F. and Chiaradonna A.; 2019: *Parametric study on 2D effect on the seismic response of alluvial valleys*. In: Silvestri F. and Moraci N. (eds), Earthquake Geotechnical Engineering for Protection and Development of Environment and Constructions, CRC Press, London, U.K.,, 8 pp., eBook ISBN: 9780429031274.

Ayoubi P., Mohammadi K. and Asimaki D.; 2021: *A systematic analysis of basin effects on surface ground motion*. Soil Dyn. Earthquake Eng., 141, 106490, doi: 10.1016/j.soildyn.2020.106490.

Bakir N. and Özkan M.Y.; 2002: *Effects of basin edge on the distribution of damage in 1995 Dinar, Turkey earthquake*. Soil Dyn. Earthquake Eng., 22, 335-345, doi: 10.1016/S0267-7261(02)00015-5.

Bard P.Y. and Bouchon M.; 1980a: *The seismic response of sediment-filled valleys, part 1. The case of incident SH waves*. Bull. Seismol. Soc. Am., 70, 1263-1286, doi: 10.1785/BSSA0700041263.

Bard P.Y. and Bouchon M.; 1980b: *The seismic response of sediment-filled valleys, part 2. The case of incident P and SV waves*. Bull. Seismol. Soc. Am., 70, 1921-1941, doi: 10.1785/BSSA0700051921.

Bard P.Y. and Bouchon M.; 1985: *The two-dimensional resonance of sediment-filled valleys*. Bull. Seismol. Soc. Am., 75, 519-541, doi: 10.1785/BSSA0750020519.

Bindi D., Luzi L., Parolai S., Di Giacomo D. and Monachesi G.; 2011: *Site effects observed in alluvial basins: the case of Norcia (central Italy)*. Bull. Earthquake Eng., 9, 1941-1959, doi: 10.1007/s10518-011-9273-3.

Bouckovalas G.D. and Papadimitriou A.G.; 2005: *Numerical evaluation of slope topography effects on seismic ground motion*. Soil Dyn. Earthquake Eng., 25, 547-558, doi: 10.1016/j.soildyn.2004.11.008.

CEN (European Committee for Standardization); 2004: *Eurocode 8: design of structures for earthquake resistance - Part 1: General rules, seismic actions and rules for buildings*. EN 1998-1:2004, Brussels, Belgium, 232 pp.

Chávez-García F.J. and Faccioli E.; 2000: *Complex site effects and building codes: making the leap*. J. Seismol., 4, 23-40, doi: 10.1023/A:1009830201929.

Chávez-García F.J., Stephenson W.R. and Rodríguez M.; 1999: *Lateral propagation effects observed at Parkway, New Zealand. A case history to compare 1D versus 2D site effects*. Bull. Seismol. Soc. Am., 89, 718-732, doi: 10.1785/BSSA0890030718.

Cornou C., Bard P.Y. and Dietrich M.; 2003: *Contribution of dense array analysis to the identification and quantification of basin-edge-induced waves, part II: application to Grenoble basin (French Alps)*. Bull. Seismol. Soc. Am., 93, 2624-2648, doi: 10.1785/0120020140.

Daniel W.W.; 1990: *Applied nonparametric statistics, 2 ed*. PWS-Kent Publishing Company, Boston, MA, USA, 635 pp.

Daniell J.E., Wenzel F., Khazai B., Santiago J.G. and Schaefer A.; 2014: *A worldwide seismic code index, country-by-country global building practice factor and socioeconomic vulnerability indices for use in earthquake loss estimation*. In: Proc. 2nd European Conference on Earthquake Engineering and Seismology, Istanbul, Turkey, 12 pp.

Davis L.L. and West L.R.; 1973: *Observed effects of topography on ground motion*. Bull. Seismol. Soc. Am., 63, 283-298, doi: 10.1785/BSSA0630010283.

Frankel A., Carver D., Cranswick E., Bice T., Sell R. and Hanson S.; 2001: *Observations of basin ground motions from a dense seismic array in San Jose, California*. Bull. Seismol. Soc. Am., 91, 1-12, doi: 10.1785/0120000071.

Graves R.W., Pitarka A. and Somerville P.G.; 1998: *Ground-motion amplification in the Santa Monica area: effects of shallow basin-edge structure*. Bull. Seismol. Soc. Am., 88, 1224-1242, doi: 10.1785/BSSA0880051224.

Hanks T.C.; 1975: *Strong ground motion of the San Fernando, California, earthquake: ground displacements*. Bull. Seismol. Soc. Am., 65, 193-225, doi: 10.1785/BSSA0650010193.

Kawase H.; 1996: *The cause of the damage belt in Kobe: "The basin-edge effect," Constructive interference of the direct S-wave with the basin-induced diffracted/Rayleigh waves*. Seismol. Res. Lett., 67, 25-34, doi: 10.1785/gssrl.67.5.25.

Kawase H. and Aki K.; 1989: *A study on the response of a soft basin for incident S, P and Raleigh waves with special reference to the long duration observed in Mexico City*. Bull. Seismol. Soc. Am., 79, 1361-1382, doi: 10.1785/BSSA0790051361.

Khanbabazadeh H. and Iyisan R.; 2014: *A numerical study on the 2D behavior of the single and layered clayey basins*. Bull. Earthquake Eng., 12, 1515-1536, doi: 10.1007/s10518-014-9590-4.

Koketsu K. and Kikuchi M.; 2000: *Propagation of seismic ground motion in the Kanto basin, Japan*. Sci., 288, 1237-1239.

Ktenidou O.J., Chávez-García F.J., Raptakis D. and Pitilakis K.D.; 2016: *Directional dependence of site effects observed near a basin edge at Aegion, Greece*. Bull. Earthquake Eng., 14, 623-645.

Lanzo G. and Pagliaroli A.; 2009: *Numerical modeling of site effects at San Giuliano di Puglia (southern Italy) during the 2002 Molise seismic sequence*. J. Geotech. Geoenviron. Eng., 135, 1295-1313, doi:10.1061/(ASCE)GT.1943-5606.0000055.

Madiai C. and Simoni G.; 2013: *Analyses of the basin geometry effects across the Aterno valley in Petogna (AQ) - Italy*. Ital. Geotech. J., 4, 24-37.

Madiai C., Facciorusso J., Baglione M. and Gargini E.; 2016: *1D versus 2D site effects from numerical analyses on a cross section at Barberino di Mugello (Tuscany, Italy)*. Procedia Eng., 158, 499-504, doi: 10.1016/j.proeng.2016.08.479.

Madiai C., Facciorusso J. and Gargini E.; 2017: *Numerical modeling of seismic site effects in a shallow alluvial basin of the northern Apennines (Italy)*. Bull. Seismol. Soc. Am., 107, 2094-2105, doi:10.1785/0120160293.

Makra K., Chávez-García F.J., Raptakis D. and Pitilakis K.; 2005: *Parametric analysis of the seismic response of a 2D sedimentary valley: implications for code implementations of complex site effects*. Soil Dyn. Earthquake Eng., 25, 303-315, doi: 10.1016/j.soildyn.2005.02.003.

Mallet R.; 1862: *Great Neapolitan earthquake of 1857 (2 vols.)*. Chapman and Hall, London, UK, 440 pp.

Meza-Fajardo K.C., Varone C., Lenti L., Martino S. and Semblat J.F.; 2019: *Surface wave quantification in a highly heterogeneous alluvial basin: case study of the Fosso di Vallerano valley, Rome, Italy*. Soil Dyn. Earthquake Eng., 120, 292-300, doi: 10.1016/j.soildyn.2019.02.008.

Ministero delle Infrastrutture e dei Trasporti (MIT); 2018: *Aggiornamento delle "Norme Tecniche per le Costruzioni".* Decreto 17 gennaio 2018*,* GU Serie generale n. 42, Suppl. Ordinario n. 8 del 20 febbraio 2018, Italy.

Paolucci R. and Morstabilini L.; 2006: *Non-dimensional site amplification functions for basin-edge effects on seismic ground motion*. In: Proc. 3rd International Symposium on the Effects of Surface Geology on Seismic Motion, Grenoble, France, paper n. 41.

Papadimitriou A.G.; 2019: *An engineering perspective on topography and valley effects on seismic ground motion*. In: Silvestri F. and Moraci N. (eds), Earthquake Geotechnical Engineering for Protection and Development of Environment and Constructions, CRC Press, London, U.K.,, 16 pp., eBook ISBN: 9780429031274.

Pitarka A., Suetsugu D. and Takenaka H.; 1996: *Elastic finite-difference modeling of strong motion in Ashigara valley for the 1990 Odawara, Japan, earthquake*. Bull. Seismol. Soc. Am., 86, 981-990, doi: 10.1785/BSSA0860040981.

Pitilakis K., Riga E., Anastasiadis A. and Makra K.; 2015: *New elastic spectra, site amplification factors and aggravation factors for complex subsurface geometry towards the improvement of EC8*. In: Proc. 6th International Conference on Earthquake Geotechnical Engineering, Christchurch, New Zealand, 11 pp., doi: 10.13140/RG.2.1.2979.2729.

Rial J.A., Saltzman N.G. and Ling H.; 1992: *Earthquake - induced resonance in sedimentary basins*. Am. Scientist, 80, 566-578.

Riga E., Makra K. and Pitilakis K.; 2016: *Aggravation factors for seismic response of sedimentary basins: a code-oriented parametric study*. Soil Dyn. Earthquake Eng., 91, 116-132, doi: 10.1016/j.soildyn.2016.09.048.

Riga E., Makra K. and Pitilakis K.; 2018: *Investigation of the effects of sediments inhomogeneity and nonlinearity on aggravation factors for sedimentary basins*. Soil Dyn. Earthquake Eng., 110, 284-299, doi: 10.1016/j.soildyn.2018.01.016.

Semblat J.F., Dangla P., Kham M. and Duval A.M.; 2002: *Seismic site effects for shallow and deep alluvial basins: in-depth motion and focusing effect*. Soil Dyn. Earthquake Eng., 22, 849-854, doi: 10.1016/S0267-7261(02)00107-0.

Semblat J.F., Kham M., Parara E., Bard P.Y., Pitilakis K., Makra K. and Raptakis D.; 2005: *Seismic wave amplification: basin geometry vs soil layering*. Soil Dyn. Earthquake Eng., 25, 529-538, doi: 10.1016/j.soildyn.2004.11.003.

STACEC S.r.l.; 2017: *LSR-2D (Local Seismic Response 2D). User manual*. <www.stacec.com>.

Stamati O., Klimis N. and Lazaridis T.; 2016: *Evidence of complex site effects and soil non-linearity numerically estimated by 2D vs 1D seismic response analyses in the city of Xanthi*. Soil Dyn. Earthquake Eng., 87, 101-115, doi: 10.1016/j.soildyn.2016.05.006.

Trifunac M.D. and Hudson D.E.; 1971: *Analysis of the Pacoima dam accelerogram - San Fernando, California, earthquake of 1971*. Bull. Seismol. Soc. Am., 61, 1393-1411, doi: 10.1785/BSSA0610051393.

Tucker B.E. and King J.L.; 1984: *Dependence of sediment-filled valley response on input amplitude and valley properties*. Bull. Seismol. Soc. Am., 74, 153-165, doi: 10.1785/BSSA0740010153.

Uzielli M., Zei M., Facciorusso J. and Madiai C.; 2019: *Probabilistic estimation of linear and volumetric strain thresholds for Italian clays*. In: Proc. 29th European Safety and Reliability Conference, Hannover, Germany, paper n. 1056.

Vessia G. and Russo S.; 2013: *Relevant features of the valley seismic response: the case study of Tuscan northern Apennine sector*. Bull. Earthquake Eng., 11, 1633-1660, doi: 10.1007/s10518-013-9456-1.

Zahradnik J. and Hron F.; 1987: *Seismic ground motion of sedimentary valleys - example La Molina, Lima, Peru*. J. Geophys., 62, 31-37.

Zhu C. and Thambiratnam D.; 2016: *Interaction of geometry and mechanical property of trapezoidal sedimentary basins with incident SH waves*. Bull. Earthquake Eng., 14, 2977-3002, doi: 10.1007/s10518-016-9938-z.

Zhu C., Chávez-García F.J., Thambiratnam D. and Gallage C.; 2018a: *Quantifying the edge-induced seismic aggravation in shallow basins relative to the 1D SH modelling*. Soil Dyn. Earthquake Eng., 115, 402-412, doi: 10.1016/j.soildyn.2018.08.025.

Zhu C., Thambiratnam D. and Gallage C.; 2018b: *Statistical analysis of the additional amplification in deep basins relative to the 1D approach*. Soil Dyn. Earthquake Eng., 104, 296-306, doi: 10.1016/j.soildyn.2017.09.003.

Zhu C., Riga E., Pitilakis K., Zhang J. and Thambiratnam D.; 2020: *Seismic aggravation in shallow basins in addition to one-dimensional site amplification*. J. Earthquake Eng., 24, 1477-1499, doi: 10.1080/13632469.2018.1472679.

Corresponding author: Giovanni Ciardi
Department of Civil and Environmental Engineering, University of Perugia
Via G. Duranti 93, 06125 Perugia, Italy
E-mail: giovanni.ciardi@unipg.it